Martian water ice clouds: A view from Mars Global Surveyor Thermal Emission Spectrometer

A. Snyder Hale,[1] L. K. Tamppari,[1] D. S. Bass,[1] and M. D. Smith[2]

Received 3 June 2009; revised 30 September 2010; accepted 20 December 2010; published 13 April 2011.

[1] We have used the Mars Global Surveyor Thermal Emission Spectrometer (MGS TES) data to map water ice clouds in the Martian atmosphere in the latitude range –60 to +60 over a period of three Martian years. We have used the same method we have previously used on Viking Infrared Thermal Mapper data in order to allow direct comparison of the cloud behavior in the Viking and MGS eras and confirmed the validity of this method by comparing it to MGS TES standard retrievals. We note that the large-scale behavior of water ice clouds is remarkably consistent, both between the Viking and the MGS eras as well as between years observed by MGS. We also compare our results to water ice absorption-only optical depths derived from TES data and show that correlation is best for type 2 water ice clouds.

Citation: Hale, A. S., L. K. Tamppari, D. S. Bass, and M. D. Smith (2011), Martian water ice clouds: A view from Mars Global Surveyor Thermal Emission Spectrometer, *J. Geophys. Res.*, *116*, E04004, doi:10.1029/2009JE003449.

1. Introduction

[2] Over the past decade there has been an increased interest in water ice clouds in the Martian atmosphere and the role they may play in the Martian water cycle. Water ice clouds in the Martian atmosphere have been inferred, historically, through observations of "blue" and "white" clouds (H. Flaugergues, cited by *Capen and Martin* [1971]) but the first positive confirmation of water ice in the atmosphere came during the Mariner 9 mission, through the Infrared Interferometer Spectrometer experiment [*Curran et al.*, 1973]. Subsequent orbital data sets have continued to show evidence for water ice clouds, with the most recent being those from Mars Global Surveyor, Mars Odyssey, Mars Express, and now Mars Reconnaissance Orbiter. Historically, these clouds were not thought to be a major contributor to the Martian water cycle or Martian atmospheric circulation. This view was originally challenged more than a decade ago by *Clancy et al.* [1996], who proposed that water ice clouds might serve as a global control on the vertical distribution of atmospheric water; similar processes operate on Earth [i.e., *DeMott et al.*, 2003]. Subsequent researchers have shown that water ice clouds are indeed ubiquitous on Mars [i.e., *Tamppari et al.*, 2000; *Pearl et al.*, 2001; *Liu et al.*, 2003; *Smith*, 2004; *Benson et al.*, 2006; *Glenar et al.*, 2003]. Additionally, cloud features that were originally thought to be absent or minor in the Viking era, such as the aphelion tropical cloud belt, have been shown more recently to be recurring and widespread [i.e., *Tamppari et al.*, 2000], a further indication that water ice is a significant contributor to Martian atmospheric dynamics and to the Martian climate, and are therefore an atmospheric feature of interest to study.

[3] As Mars scientists, we should be interested in water ice clouds because they are an important part of the Martian water cycle, though they comprise a relatively small volume of Martian atmospheric water [*Montmessin et al.*, 2004]. Unlike other important reservoirs, such as the polar caps, clouds can be used to track the transport of this water over distances of potentially thousands of kilometers [*Montmessin et al.*, 2004]. Their seasonal and interannual patterns therefore hold important clues to the long time scale character of water transport on Mars. For example, Mars experiences aphelion during northern summer, and due to the elliptical nature of the Martian orbit, this means the northern summer is cooler than the southern summer. Not surprisingly, therefore, we see more water ice clouds in northern summer (in fact, we observe a prominent equatorial belt of water ice clouds) than in southern. The ice particles in these clouds may in turn settle gravitationally, scavenging dust from the atmosphere, and therefore reduce its radiative heating capacity [*Clancy et al.*, 1996], causing a feedback loop which may help explain why Mars's northern hemisphere is wetter than its southern (another factor contributing to Mars's northern hemisphere being wetter is that the southern summer Hadley cell is stronger than the northern [*Liu et al.*, 2002]). Whether or not these processes are ongoing year in and year out (and decade in and decade out) is also an important consideration. Are we observing a planet with a stable water cycle, or one where the water cycle and climate are rapidly changing? Studies, such as this one, which observe clouds behavior over long time scales are key to answering this question.

[4] Data from spacecraft at Mars are the most powerful tool available to the Mars scientist in studying water ice cloud climate and behavior, and there is a wealth of data available to the Mars scientist at present. Archived data are

[1]Jet Propulsion Laboratory, California Institute of Technology, Pasadena, California, USA.
[2]NASA Goddard Space Flight Center, Greenbelt, Maryland, USA.

Copyright 2011 by the American Geophysical Union.
0148-0227/11/2009JE003449

available from Mariner 9, Viking, Mars Pathfinder, Mars Global Surveyor, Phoenix, and are currently being acquired from Mars Odyssey and Mars Express, as well as the Mars Exploration Rovers and Mars Reconnaissance Orbiter. This wealth of data allows us to get a picture of Mars and its weather on time scales of decades, as opposed to simply years. However, great care must be taken in comparing data from one instrument and spacecraft to that from another. Instrumental or observational effects could be interpreted as legitimate climate change, or, conversely, could mask real climatic processes. Therefore, it is important to examine data sets that are as similar as possible using techniques as similar as possible when looking over long (in terms of spacecraft record) time scales; the ideal comparison would be done using data acquired from the same instrument and processed in the same manner, though of course this is not always possible.

[5] In this paper we present a comparison of two spacecraft data sets, and we have attempted to conduct that comparison in the most "apples to apples" way as possible. We extend the work of *Tamppari et al.* [2000], which used Viking Infrared Thermal Mapper (IRTM) data to examine behavior of Martian water ice clouds, to the Mars Global Surveyor Thermal Emission Spectrometer (MGS TES) data set. The two goals of this work are (1) to validate the cloud detection method of *Tamppari et al.* [2000] by comparing this method's results as applied to TES data to the TES opacities that are publicly available and (2) to compare the cloud climatology between the Viking and MGS eras using the same technique on both data sets.

[6] TES was able to map Mars with far more complete spatial coverage than Viking (and for a longer span of time), and comparing these two data sets will allow us to study the behavior of the Martian atmosphere during two periods separated by nearly 15 Martian years with high fidelity, though the reader should keep in mind that 15 Martian years have not been continuously monitored. Though TES had a much higher spectral resolution than the Viking IRTM, we can convolve the TES data to the IRTM band shapes, and thus generate synthetic "IRTM data" from the TES instrument. This data can then be processed by the exact same method of *Tamppari et al.* [2000]. We can then use these TES-derived maps to directly assess differences in climate and weather exhibited by the water ice clouds between the MGS and Viking eras. We have also, as part of this work, compared our maps to maps of water ice opacity derived from TES utilizing its full spectral capability, in order to assess the validity of the IRTM methodology.

[7] Section 2 of this paper provides a brief description of the MGS TES and Viking IRTM instruments and data, and it summarizes our cloud retrieval method (that of *Tamppari et al.* [2000]). Section 3 compares our TES era temperature-differenced results to those of *Smith* [2004], who extracted water ice opacities directly from TES data. Section 4 compares our TES era temperature-differenced results to those obtained from the Viking IRTM data set. Finally, section 5 contains our conclusions.

2. IRTM and TES Instruments and Data: Temperature-Differencing Cloud Retrieval Method

2.1. IRTM Instrument and Data

[8] The Viking IRTM instrument has been described previously [*Chase et al.*, 1978]; a brief description is given here. The Viking IRTM observed thermal emission from Mars in 5 wavelength bands, commonly called T_7, T_9, T_{11}, T_{15} and T_{20}. The number corresponds to the central wavelength (in microns) of each band. T_{15} is the atmospheric carbon dioxide sensing band; the other channels were designed to sense the Martian surface. Each Viking orbiter carried an IRTM instrument, and between the two spacecraft, slightly more than two Martian years worth of data were acquired, an excellent record which was not surpassed until the Mars Global Surveyor mission twenty years later. Viking, unlike more recent NASA Mars missions, did not have a fixed polar near-circular orbit, meaning that longitudinal coverage over a short period of time in the IRTM data set is not as complete as that achieved by later instruments such as MGS TES or Odyssey's THEMIS, though far greater diurnal coverage was achieved.

2.2. TES Instrument and Data

[9] The TES instrument began orbiting Mars in 1997, and is described in detail by *Christensen et al.* [2001]. A brief description is given here. TES is an uncooled infrared Michelson interferometric spectrometer, and contains broadband radiometers as well. The spectral range of the instrument is approximately 6 to 50 μm (with either 150 or 300 channels, depending on instrument mode), while the radiometers are sensitive in the visible to near IR (0.3–2.9 μm) and the far IR (5.1–150 μm). We use spectrometer data in this study.

[10] As TES samples at a much higher spectral resolution than did IRTM, TES data can be convolved to IRTM resolution in order to use the method presented by *Tamppari et al.* [2000] for analysis. Therefore, we use spectrometer data that has been convolved to the IRTM band passes, and this synthetic "IRTM data" can then be manipulated identically to the actual Viking IRTM data. Data included in this study span both the nominal MGS mission and the extended mission, and were obtained between 1998 and 2004. Data were retrieved directly from the TES team's public database (http://tes.asu.edu/data_archive.html) using their *vanilla* software.

[11] It should be noted that due to the fixed 1400 local time (LT) nature of MGS's orbit, TES data are concentrated in a narrow time frame around 1400 LT (1330–1430 local solar time (LST)) whereas the IRTM data cover a large range of diurnal times. For Viking IRTM, we restricted our data analyzed to local solar time 1000 LT to 1400 LT, and also to the latitude range –60° to +60° and to emission angles from 0° to 60°. Martian cloud features have been observed to have some diurnal variability, especially the aphelion cloud belt [*Wolff et al.*, 1999; *Tamppari et al.*, 2003]. *Wolff et al.* [1999], using Hubble Space Telescope observations, found that the midday time frame was the least cloudy overall, but that the aphelion cloud belt was observed even during this time of day. Similarly, *Tamppari et al.* [2003] found the midday timeframe to be the least cloudy in the springtime hemisphere, but during late summer in the southern hemisphere, cloud extent decreased from midday (1000 LT to 1400 LT) to afternoon (1400 LT to 1700 LT). In all cases, major cloud features remained observable. We have chosen to use the 1000 to 1400 LST time constraint for the Viking data because it compares best to the local time of day for which the TES data were taken, yields sufficient data for analysis, and also provides the possibility for the greatest temperature contrast between water ice clouds and surface,

maximizing our chances of detecting clouds [*Tamppari et al.*, 2000]. We investigated restricting the IRTM data to 1300 LST to 1500 LST, but the data available for examination decreased dramatically. Because we are investigating large-scale climatological change (or lack thereof) between the MGS and Viking eras, not small-scale weather features, and previous diurnal studies have shown that the major climatological features are still present at earlier and later times, while there may be diurnal effects in cloud occurrence, we have chosen to maintain the use of IRTM data between 1000 LT and 1400 LT for this study.

[12] Finally, the range of emission angles seen by TES is much narrower than that seen by IRTM as well (emission angle ≤ 1 degree, typically), whereas the emission angles seen by Viking IRTM are highly variable. The implications of this are discussed in section 2.7.

2.3. Temperature-Differencing Method of *Tamppari et al.* [2000]

[13] This method is discussed in great detail by *Tamppari et al.* [2000, Figure 3], and to a lesser degree by *Tamppari et al.* [2003]; however, we will also give a summary here. This method makes use of the water ice absorption feature that spans the spectral range from 10 to 30 μm. The 11 μm IRTM channel is more strongly affected by this absorption than is the 20 μm channel, so by comparing the signal in the 11 μm channel to that in the 20 μm channel, we can assess whether a water ice cloud is present (Figure 1). Since the 11 μm channel is within the water ice absorption band [e.g., *Curran et al.*, 1973], when a water ice cloud is present, the T_{11} channel will sense photons coming from the surface that are not scattered out of the line of sight by a water ice cloud or those that are absorbed by the water ice cloud and reradiated at the cloud temperature. Thus, T_{11} will have a colder brightness temperature than $T_{20,}$ which is not as sensitive to this water ice absorption feature. Therefore, when the T_{20} signal is subtracted from the T_{11}, negative values are indicative of water ice clouds. This method works well when we restrict ourselves to only using data taken at midday when we expect the surface to be significantly warmer than water ice clouds. This method will not erroneously detect cold atmospheric temperature in the absence of water ice cloud because in that case there is no absorption and reradiation of surface emission photons at 11 microns.

[14] Other researchers have attempted this same spectral comparison prior to *Tamppari et al.* [2000] [*Christensen and Zurek*, 1984], but ended up mapping surface as well as atmospheric features. This was caused by wavelength-dependent surface emission across the face of Mars. More specifically, in the thermal wavelength regime, such an instrument observes atmospheric emission, surface emission, and surface and atmospheric emission scattered into the line of sight together. All of these are also of course attenuated over the line of sight by atmospheric absorption and scattering. Based on the results of his earlier 1984 paper, *Christensen* [1998] provided surface emissivity maps of Mars based on Viking observations, which allowed for these effects to be accounted for. *Tamppari et al.* [2000] accounted for the effect of the wavelength-dependent surface emissivity on the IRTM brightness temperatures by using them with a surface model developed by *Paige et al.* [1994], which uses a one dimensional radiative transfer code to model the expected surface thermal emission in the IRTM bands throughout the Martian year; the *Christensen* [1998] emissivities are an input parameter to this surface model. Paige's model requires as additional input the surface albedo and thermal inertia, and specifically computes the expected T_{20} radiance. Expected values for the other IRTM channels are then computed similarly, and can be compared to the T_{20} value. In our case, of course, we subtract the T_{20} value from the T_{11} value in order to determine an expected "no-cloud" T_{11}–T_{20} value. When this modeled surface contribution is subtracted from the actual observed T_{11}–T_{20} signal, atmospheric features can be confidently mapped. We can represent this process mathematically thus [from *Tamppari et al.*, 2000]:

$$\Delta T_{c+S} - \Delta T_S = \Delta w \leq -1 \text{ K} \quad (1)$$

where ΔT_{c+S} is the observed temperature difference (in Kelvin) containing both cloud and surface contribution to the observed radiance, and ΔT_S is the modeled no-cloud surface temperature difference (in Kelvin), which is generally small, and Δw is the result which is then compared to our threshold of −1 K. The value of minus one as our cloud detection threshold is taken from *Tamppari et al.* [2000, section 3.2].

[15] It should be noted that the *Paige et al.* [1994] model has only a constant correction for greenhouse heating of the Martian surface (a 2% radiative feedback), and therefore the modeled surface temperatures may be somewhat colder or warmer than the actual surface temperatures, depending on the actual state of the atmosphere. *Wilson et al.* [2007] showed that the greenhouse heating effect is much more pronounced at night, and outside of major dust events the daytime effects of greenhouse heating are minor. We therefore believe we can continue using Paige's model and its constant correction without affecting the validity of our results.

[16] The temperature-differencing cloud detection method is very robust, and is not dependent on an atmospheric model, though it is of course dependent on the fidelity of the *Paige et al.* [1994] surface model. This model is in turn dependent on the accuracy of emissivities, albedos, and thermal inertias fed into it. There are some cases the Tamppari method currently cannot treat, the most important being that it cannot map clouds over surfaces whose temperature is at or colder than the temperature of atmospheric water ice, since the method relies on mapping a colder, absorbing cloud (detected via T_{11}) over a warmer surface (detected via T_{20}), creating the T_{11}–T_{20} temperature difference. Therefore, clouds may not be able to be confidently mapped over the Martian poles with this method, though they may obviously be present. In the work of *Tamppari et al.* [2000] and in this study we explicitly ignore areas of Mars for which the surface model indicates temperatures are colder than CO_2 ice. We also only use daytime data, as the nighttime data (both TES and IRTM) are often quite noisy, and at night temperature inversions may occur where the atmosphere is actually warmer than the surface.

[17] It is also possible, though unlikely, that dust signatures may be confused with water ice signatures, and hence, inadvertently be mapped as water ice clouds. *Tamppari et al.* [2000] considered this possibility extensively, and concluded that only in cases where $\tau_{\text{vis, dust}} > 0.3$ and the surface spectral emissivity difference, ε_{11}- ε_{20}, is greater than zero is

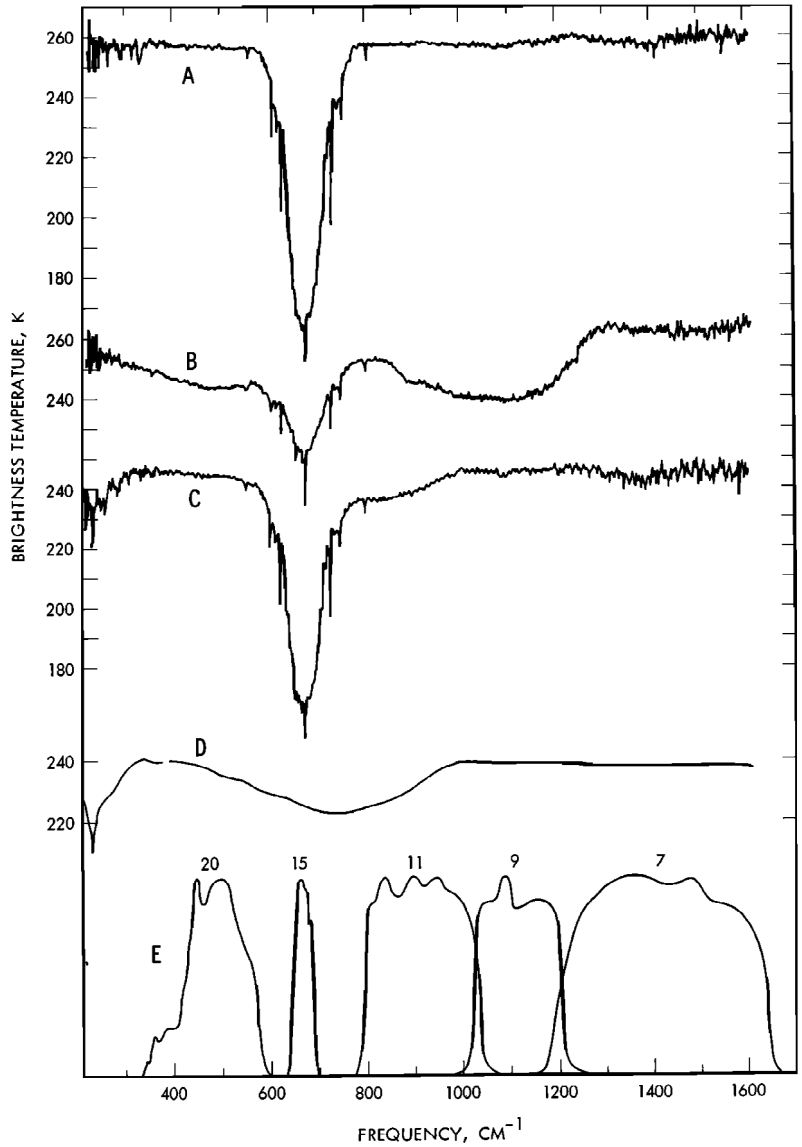

Figure 1. (Figure and caption are taken from *Tamppari et al.* [2000] Mariner 9 infrared interferometer spectrometer (IRIS) spectra with Viking orbiter Infrared Thermal Mapper (IRTM) band passes [from *Martin et al.*, 1979].) (a) A typical spectrum of Mars with no atmospheric water ice or dust contamination. The strong absorption at 667 cm^{-1} is due to the vibrational band of gaseous CO_2 in the Martian atmosphere. (b) A spectrum showing dust absorption centered near 1100 cm^{-1} (9 μm) during a global dust storm and (c) a spectrum showing water ice absorption (shoulder near 800–900 cm^{-1}) due to a cloud over Tharsis. (d) A theoretical model for the water ice cloud in Figure 1c [*Curran et al.*, 1973]. (e) The IRTM band passes, labeled above with their micrometer designation. The *x* axis is frequency (cm^{-1}), and the *y* axis shows different brightness temperatures scales (K) for the different spectra.

confusing dust with water ice a risk. In the maps shown subsequently in this manuscript, areas with high dust opacities ($\tau_{\text{vis, dust}} > 0.3$) as retrieved from the TES teams' database have been explicitly ignored and are shown as black.

2.4. TES Data Used

[18] As previously stated, for this study, we used synthetic T_{11} and T_{20} data directly from the TES team's database. We retrieved data in temporal bins of 15 degrees of L_s, for the latitude range –60° to +60° (all longitudes were included) for three Martian years. Fifteen degrees was chosen as the temporal bin for consistency with *Tamppari et al.* [2000], who chose this number to ensure enough data were available to cover all longitudes, given the elliptical Viking orbit. The three years chosen correspond to Mars years 24, 25, and 26, after *Clancy et al.* [2000]. We then used IDL code adapted by our team from code originally developed at UCLA (M. Sullivan, private communication, 2003) to bin the data spatially in 2 × 2 degree bins, subtract the modeled surface emission [*Paige et al.*, 1994], and map the output.

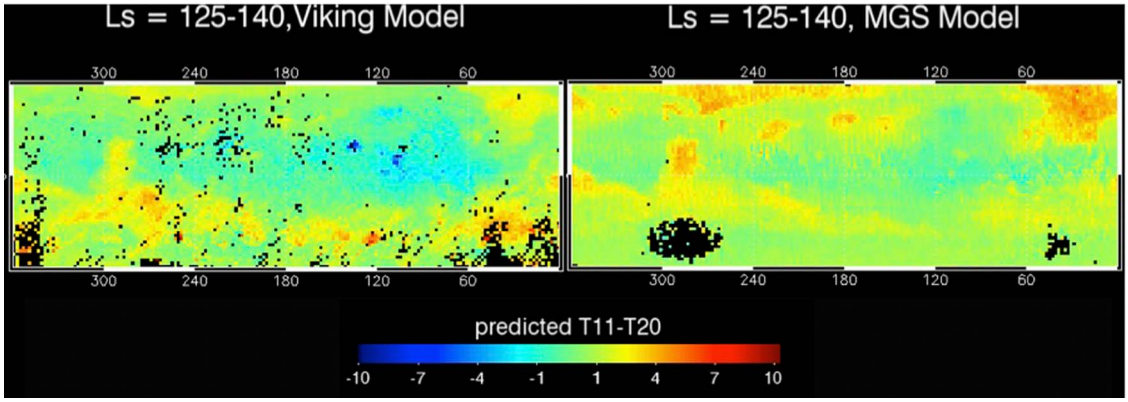

Figure 2. (left) The *Paige et al.* [1994] surface model using Viking-derived input parameters (emissivity, albedo, and thermal inertia). (right) The same surface model using MGS TES-derived input parameters. The Viking-derived model has more sporadically distributed missing data and also shows evidence of atmospheric contamination over the Tharsis volcanoes and the surrounding areas. The effects of this atmospheric contamination on cloud mapping are mainly conservative, i.e., the amount of cloud mapped using such a surface model would be a lower limit on the amount of cloud actually present. The MGS-based model has data missing at Hellas and Argyre because the surface model becomes numerically unstable there due to low input emissivities, so these areas are explicitly excluded.

In our maps, black areas indicate areas without data (or areas with corresponding TES dust opacities too high to yield reliable results), white areas indicate that data were present, but no clouds were detected, and clouds are indicated with color, with blue being a weak detection and red being a strong one. As with Tamppari's earlier work, we take as our "cloud cutoff point" to be a Δw signal of −1 K (in general, on plots, we will use T_{11}–T_{20} to mean the full processing, Δw, as a shorthand reminder that it is a temperature difference between the 11 and 20 micron channels). That is, any value of Δw equal to or less than −1 K is indicative of water ice cloud, and any value greater than −1 K indicates a lack of cloud. It should be noted that, a priori, we assign no quantitative significance to particular values of Δw in terms of volume of ice present. More negative values of Δw may mean more ice is present, but they also may indicate a colder or higher cloud, for example. The relationship between opacity and the Δw temperature difference is discussed further in section 3.

2.5. Surface Model: Effect of Viking Era Versus MGS Era Input Parameters

[19] As previously stated, the surface model we use requires as input the surface emissivity, the surface albedo, and the thermal inertia. Obviously, these quantities must be provided at the desired spatial resolution (in our case 2 × 2 degrees). We therefore use values derived from spacecraft measurements, as opposed to those derived from telescopic observations. In the work of *Tamppari et al.* [2000], these input quantities were derived from the following sources: emissivities were from *Christensen* [1998], surface albedos from *Pleskot and Miner* [1981], and thermal inertias from *Palluconi and Kieffer* [1981]. Some newer data sets are now available, however. We have generated new surface model output using emissivities from *Christensen* [1998], albedos from *Christensen* [1998], and thermal inertias from *Putzig et al.* [2003]; these latter two quantities were derived from MGS TES observations. Figure 2 shows the modeled surface emission at L_s = 125–140° with both the older Viking-derived input parameters, and the newer TES-derived ones.

[20] The Viking-derived surface model output has more sporadically distributed missing data than the MGS-derived output, which has missing data concentrated mainly in the Hellas basin. It should be noted that this missing data in Hellas is not due to incompleteness in the input data sets, but is instead due to the fact that model itself becomes unstable in Hellas with the MGS-derived input parameters, due to very low emissivities recorded there. These emissivities likely do not reflect the true state of the surface in the Hellas basin, but in all likelihood are due to an atmospheric contribution. We have therefore chosen to explicitly exclude the unstable region. The Viking-derived surface model output also has, generally speaking, lower overall values of T_{11}–T_{20}, excepting some areas in the southern hemisphere, and also appears to contain more spurious atmospheric "contamination." This contamination may be inferred from the very negative values of T_{11}–T_{20} seen in Tharsis and it surroundings. Low surficial T_{11}–T_{20} values should occur over regions of low thermal inertia and/or high albedo; these qualities are present in the Tharsis region [*Arvidson et al.*, 2002], but they are regionwide. The signal we see, however, is concentrated at the tops of the volcanoes themselves, an area where water ice clouds are frequently present [i.e., *Wang and Ingersoll*, 2002]. This atmospheric contribution to the surface model's output is incorporated into the model via the emissivities, albedo and thermal inertias, and indicate that atmospheric effects were likely not completely accounted for when these quantities were originally derived. Fortunately, however, atmospheric contamination in the surface model output has an effect than is in general conservative. That is, if surface model-predicted T_{11}–T_{20} values are lower than they should be due to atmospheric contribution to the surface model, this means a stronger T_{11}–T_{20} signal is needed to have a positive cloud detection. Therefore, clouds mapped

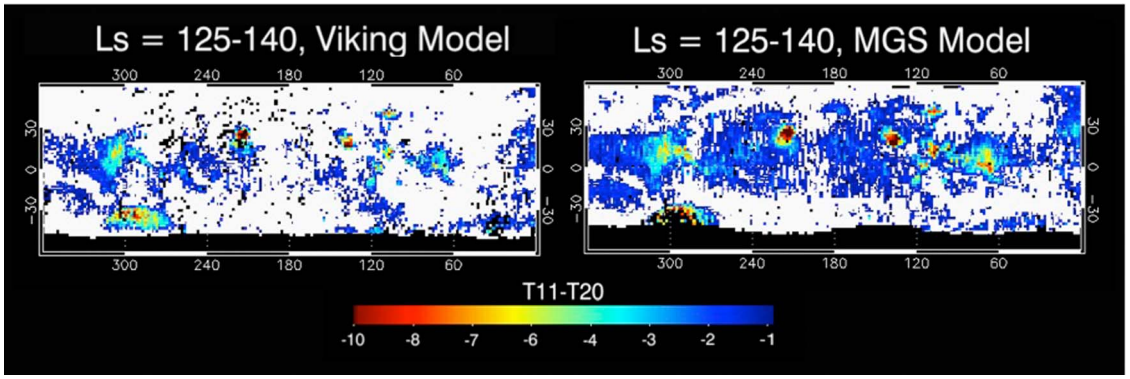

Figure 3. (left) A cloud map generated from MGS TES data (Mars year 25, L_s = 125–140°) using the Viking-derived surface model for surface subtraction. (right) A map generated from the same data, but using the MGS-derived surface model for surface subtraction. Figure 3 (right) shows more extensive cloud and also stronger cloud signatures overall. Here, T_{11}–T_{20} is really Δw, the full processing (see text).

with this sort of contamination in the surface model are a conservative lower limit on the amount of cloud actually present. This effect is easily seen in Figure 3, where we compare a cloud map generated using the same TES data with the modeled Viking-derived surface emission and the modeled TES-derived surface emission. The Viking-derived model shows less areal extent of water ice cloud overall, and the cloud signatures present are typically weaker, especially over Valles Marineris and Tharsis.

[21] We are therefore left with a choice: which surface model output to use? For temporal consistency, it makes sense to use the MGS TES-derived model output with TES data; that surface model output also has less missing data (though the missing data are strongly concentrated in Hellas only), and, most importantly, shows less evidence for atmospheric contamination than the Viking-derived model output. For these last two reasons, as well as a desire to facilitate direct and simple comparisons between the two eras, we have chosen to also regenerate the Viking maps with the MGS-derived modeled surface emission. This removes some of the conservatism of the results, but we feel it is the best choice. To use the Viking-derived model output with both data sets would also allow for direct comparison of our generated maps, but those maps would be less spatially complete and, due to the atmospheric contribution to the surface model, we believe they would present a less accurate picture of the true state of water ice in the Martian atmosphere.

2.6. Effect on Previous Viking Results

[22] Our use of a new surface model changes somewhat the results originally presented by *Tamppari et al.* [2000] for the Viking era. Mainly, the effect is one of increasing the prevalence of weak signal ($\Delta w > -2$ K) water ice clouds. An example may be seen in Figure 4. Figure 4 (left) shows a map generated from Viking IRTM data with the Viking-derived modeled temperature difference; Figure 4 (right) shows a map of the same data using the MGS-derived modeled surface. The areal extent of weak signal water ice clouds is greatly increased with the MGS surface model map, as expected, and the strength of cloud signatures in strong signal areas is increased (that is, the strong signal areas show

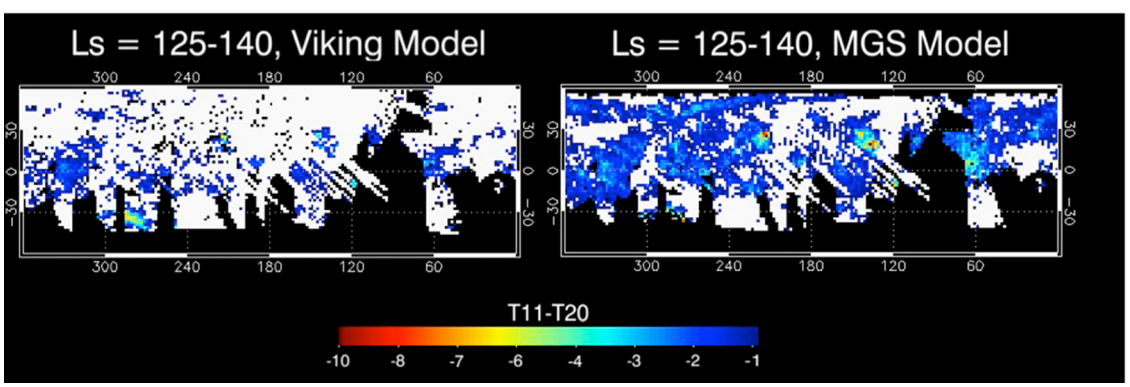

Figure 4. (left) A map generated from Viking IRTM data for L_s = 125–140° (Viking year 1) using a Viking-derived model surface. (right) A map generated from the same data using an MGS-derived surface model. As expected, low-signal clouds are more extensive in the MGS model case, and areas with strong signal show that signal strengthened. Here, T_{11}–T_{20} is really Δw, the full processing (see text).

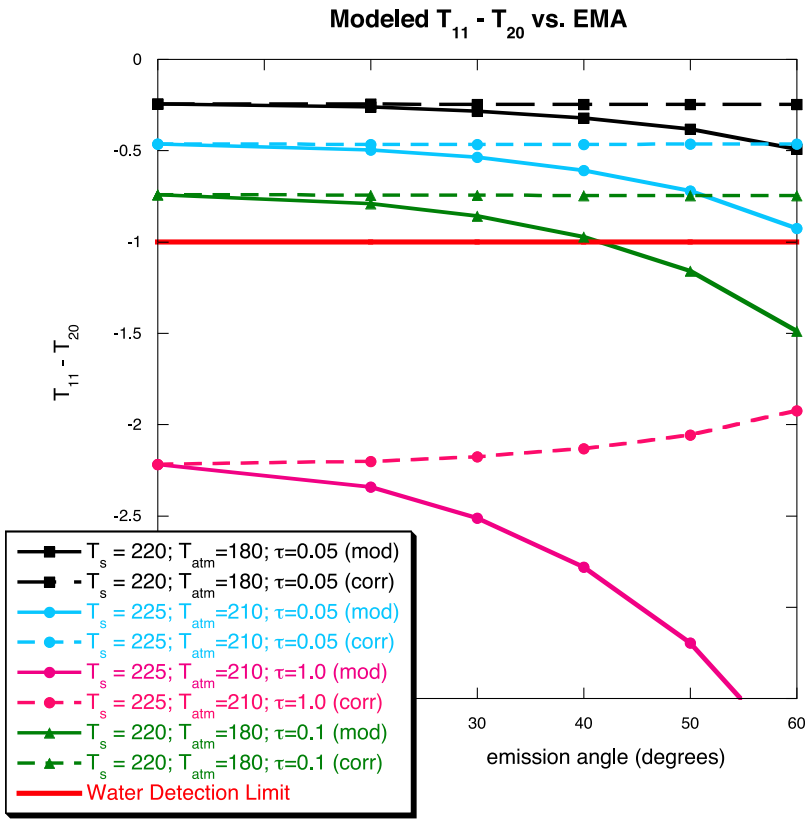

Figure 5. Plot of representative modeled T_{11}–T_{20} temperature differences (in K) for a variety of water ice cloud temperatures and opacities and surface temperatures as a function of viewing emission angle (EMA). T_s is the surface temperature used, T_{atm} is the temperature of the cloud used, and τ is the visible opacity used in each model case. The solid lines represent a fit to the model output, which was produced every 10° emission angle, and the dashed lines represent the "corrected" model output (see text). The solid red line represents our detection threshold for classifying T_{11}–T_{20} as a cloud, −1 K. The model was run for the ranges: 210 K < T_s < 255 K (based on IRTM surface temperatures), 175 K < T_{atm} < 220 K (based on modeling of the temperature of the cloud condensation height using TES water vapor data and atmospheric temperature profile data; *Pankine et al.* [2010]), and 0.05 < τ_{vis} < 1.5 (based on TES observed infrared water ice opacities, converted to visible).

values that are more negative when using the MGS-derived surface map, as opposed to the Viking-derived one). These trends are repeated in all Viking maps relative to the results presented by *Tamppari et al.* [2000], indicating that water ice may be more widespread and prevalent in the Martian atmosphere than previously thought. Large-scale seasonal cloud behaviors, such as the appearance of the aphelion cloud belt in northern summer, and the appearance and disappearance of the polar hoods, remain the same as observed by *Tamppari et al.* [2000]; that is, the picture of seasonal behavior of Martian water ice clouds presented in that work remains unchanged.

2.7. Effect of Emission Angle on Viking Observations

[23] In the work of *Tamppari et al.* [2000], the effects of variable emission angle were not explicitly accounted for, though the data examined were restricted to emission angles less than 60 degrees. However, in this work we will be comparing Viking data to MGS TES data, and the TES data presented here were all acquired at an emission angle close to zero (unlike the Viking IRTM data, which were acquired at a variety of emission angles). We have therefore explored how emission angle affects our analysis in order to explicitly account for it.

[24] The reader should note that our quantity of interest is a difference of two brightness temperatures, which themselves are calculated from data that is averaged both spatially (2 × 2 degrees of latitude and longitude) and temporally (15 degrees of L_s); our method explicitly does not examine individual radiances, nor even individual temperature measurements. As such, the dependence of our result on emission angle variation may be swamped by other effects.

[25] To assess the affect of emission angle, we modeled the T_{11}–T_{20} signature of water ice clouds using a one dimensional (1-D) radiative transfer model originally developed by *Paige et al.* [1994] (the same model discussed in section 2.3). In section 2.3 we discussed using this model in the "cloud-free" mode to generate T_{11} and T_{20} values that would result from the surface contributions alone. By adding water ice clouds to this model, it allowed us to explore how the expected T_{11}–T_{20} value would change over a range of emission angles for a variety of realistic water ice opacities,

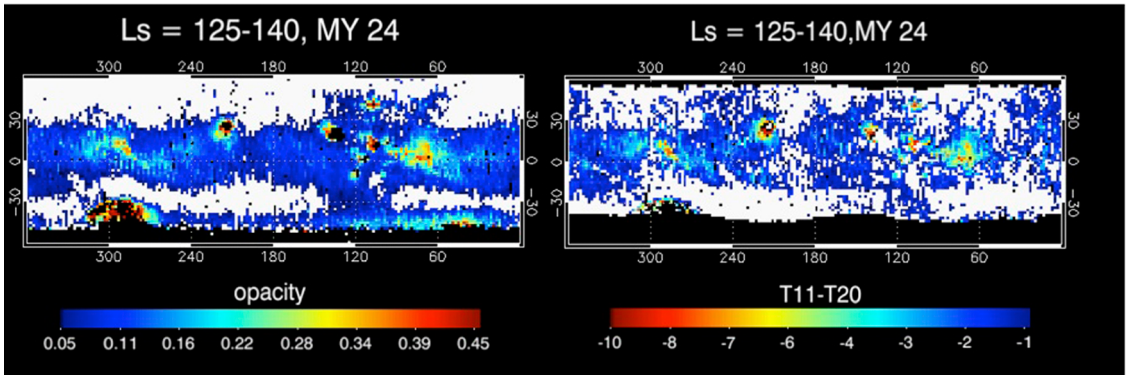

Figure 6. (left) TES-derived water ice opacities for L_s = 125–140° in the second MGS mapping year (Mars year 24). (right) The same time period mapped with our temperature-differencing method. Here, T_{11}–T_{20} is really Δw, the full processing (see text). The temperature-differencing method shows more clouds at high northern latitudes, but patchier cloud cover overall than the TES-derived opacities. However, main features such as the aphelion cloud belt and the stronger signal over the volcanoes is preserved.

cloud temperatures, and surface temperatures. For this analysis, we ran the model with unit surface emissivities. From this model output we then derived an empirical correction

$$(T_{11} - T_{20})_{\text{corrected}} = (T_{11} - T_{20})_{\text{raw}} \left(\cos(\text{ema})^{0.997}\right) \qquad (2)$$

to the IRTM data set that corrects the T_{11}–T_{20} quantity from its nonzero emission angle value back to an expected value at zero degrees emission. That is, we calculate what we expect IRTM would have seen from the atmosphere had the data been acquired at zero degrees emission, as the MGS TES data were. The modeled T_{11}–T_{20} value, for a given water ice cloud opacity and temperature and surface temperature, decreased with increasing emission angle (Figure 5). The cosine function fit was found to correct the data taken at higher emission angles back to zero degrees emission reasonably well (Figure 5).

[26] To assess this correction as applied to the Viking data, we examined histograms of our fully processed Viking data (Δw), binned in 2 × 2 degree spatial bins and averaged over all seasons, but separated into 10 degree bins of emission angle. A small shift in the peak with emission angle was seen in the uncorrected data whereas the corrected data showed less of a shift. To further validate our correction, we examined data from the EPF sequence taken on Viking orbit 42, which we determined contained water ice clouds detected via our differencing method. While the scatter in Δw values is large, they show a trend toward more negative values in the higher emission angles in the uncorrected data set, which become less negative in the corrected data set, as expected based on our modeling. As a result of the analysis described here, we chose to use this corrected Viking data in this study.

3. TES-Derived Water Ice Opacities Compared to Temperature-Differencing Method

[27] Water ice opacities (strictly speaking, absorption-only optical depths) may be retrieved directly from the TES database. These opacities are derived after the method of *Pearl et al.* [2001] and *Smith* [2004]. In short, Smith and Pearl solve for column integrated pure absorber opacities as a function of wavelength by numerically solving the radiative transfer equation for a plane parallel nonscattering atmosphere. Inputs to the procedure include spectral radiances, surface pressure, and surface and atmospheric temperatures, which must be calculated or assumed. The contribution of water ice, dust, and nonunit surface emissivity to the total opacity are then calculated by fitting predetermined spectral shapes to the total opacity. In the work of *Pearl et al.* [2001] these absorbers were assumed to be well mixed, though this assumption is not continued in Smith's later work, or in the data we show here. Contribution to the uncertainty of their calculated value includes calibration errors, instrument noise, errors in the inputs, and the assumption that the absorbers have fixed spectral shapes. The magnitude of these uncertainties is inversely proportional to the thermal contrast between the surface and the atmosphere in the daytime data set, and retrievals become noisy and uncertain over very cold surfaces (T < 220 K). The daytime data shown here have an error of approximately 0.05, or 10%, whichever is larger [*Smith*, 2004].

[28] We compared the retrieved water ice opacities for all periods to the water ice cloud signature calculated with our method. The agreement between the two methods (each detects a water ice cloud) is quite good, though occasionally there are discrepancies in low-signal areas. An example opacity map is shown in Figure 6 (left), with the same period mapped with our method shown in Figure 6 (right) for comparison. Both show the presence of the tropical cloud belt, but our method maps more low-signal cloud at high northern latitudes, whereas the opacity retrieval shows more cloud at high southern latitudes (though the southernmost extent of the data shown is greater in Figure 6, left). Both methods show strong cloud signatures over topographic highs and in Valles Marineris.

[29] Figure 7 shows correlation plots comparing our temperature-differenced data with the TES opacities. We have chosen these values of L_s shown in order to compare times of differing cloud behavior. The L_s = 125–140° range

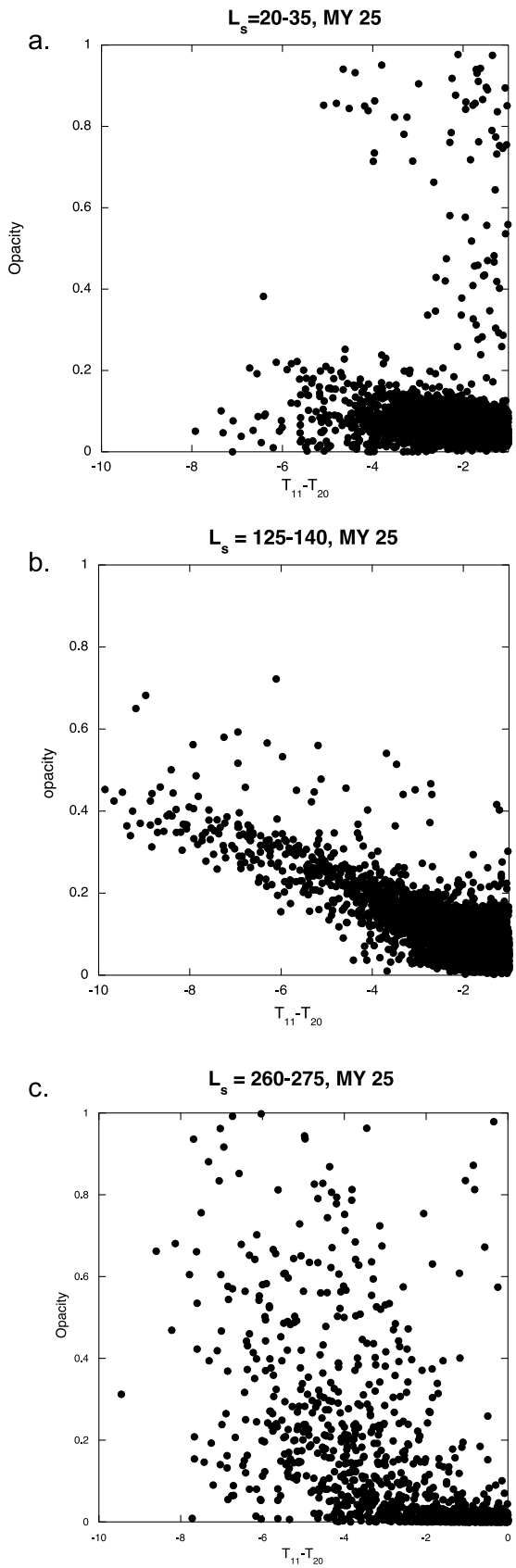

shows the aphelion cloud belt; the L_s = 260–275° shows a time with few clouds excepting the north polar hood, and the L_s = 20–35° range shows a time with widespread low-signal clouds. Only data from one Mars year are shown to keep the plots less busy; however, other years show similar behavior. A linear correlation is clearly seen in the L_s = 125–140° time period, the time showing primarily aphelion cloud belt clouds, with less correlation seen in L_s = 20–35°. *Clancy et al.* [2003] showed that aphelion cloud belt clouds are distinctly different from other Martian water ice clouds. Specifically, clouds in the aphelion cloud belt contain larger particles, and have different scattering characteristics (less backscattering and more side scattering) than other Martian water ice clouds. We can therefore infer that the stronger (more negative) signal from our temperature-differencing method is indicative of higher opacity clouds in cases where ice particles are large and exhibit less backscattering, such as the aphelion cloud belt.

[30] Correlation between the two methods is worst in the case of polar hood clouds (L_s = 260–275°) implying a more complicated relationship between the opacity and the temperature-differencing methods. A more negative T_{11}–T_{20} (or Δw, as the full processing was done here) difference is either due to a higher-opacity cloud or a colder cloud, for the same surface temperature. Polar hood clouds exist in a colder atmosphere than equatorial clouds and there may be more water available at polar latitudes; these facts may be contributing to both higher-opacity clouds and clouds at an atmospheric altitude with colder temperatures yielding the large scatter seen in our correlation plots. The opacity retrievals for L_s = 260–275° show, in general, stronger signal than our method, and our method shows more diffuse low-signal cloud cover as well. Generally speaking, however, we can infer that our method's results agree well with water ice opacity retrievals in terms of detecting clouds, especially in tropical zones. We therefore conclude that our temperature-differencing method, when applied to TES data is a valid method for mapping water ice cloud climatology in the Martian atmosphere.

4. MGS TES Temperature-Differenced Results in Comparison to Viking IRTM Results

[31] The TES data set covers all 360° longitude in a shorter period of time than was achieved with Viking, and also covers a longer record in time (over three Martian years). Due to MGS's fixed time orbit the diurnal coverage offered by TES is not nearly as complete as that seen by Viking IRTM, however. All MGS cloud maps are presented in Figures 8a–8c, with the newly generated Viking maps for comparison.

Figure 7. (a) A correlation plot of TES opacity retrievals with our T_{11}–T_{20} data for L_s = 20–35°, Mars year 25. (b and c) The same year's data, but for the labeled L_s ranges. Here, T_{11}–T_{20} is really Δw, the full processing (see text). The clearest linear trend is seen in L_s = 125–140°, a time when the most prominent cloud feature is the aphelion cloud belt. The worst correlation is seen in L_s = 260–275°, a time when these clouds are completely absent.

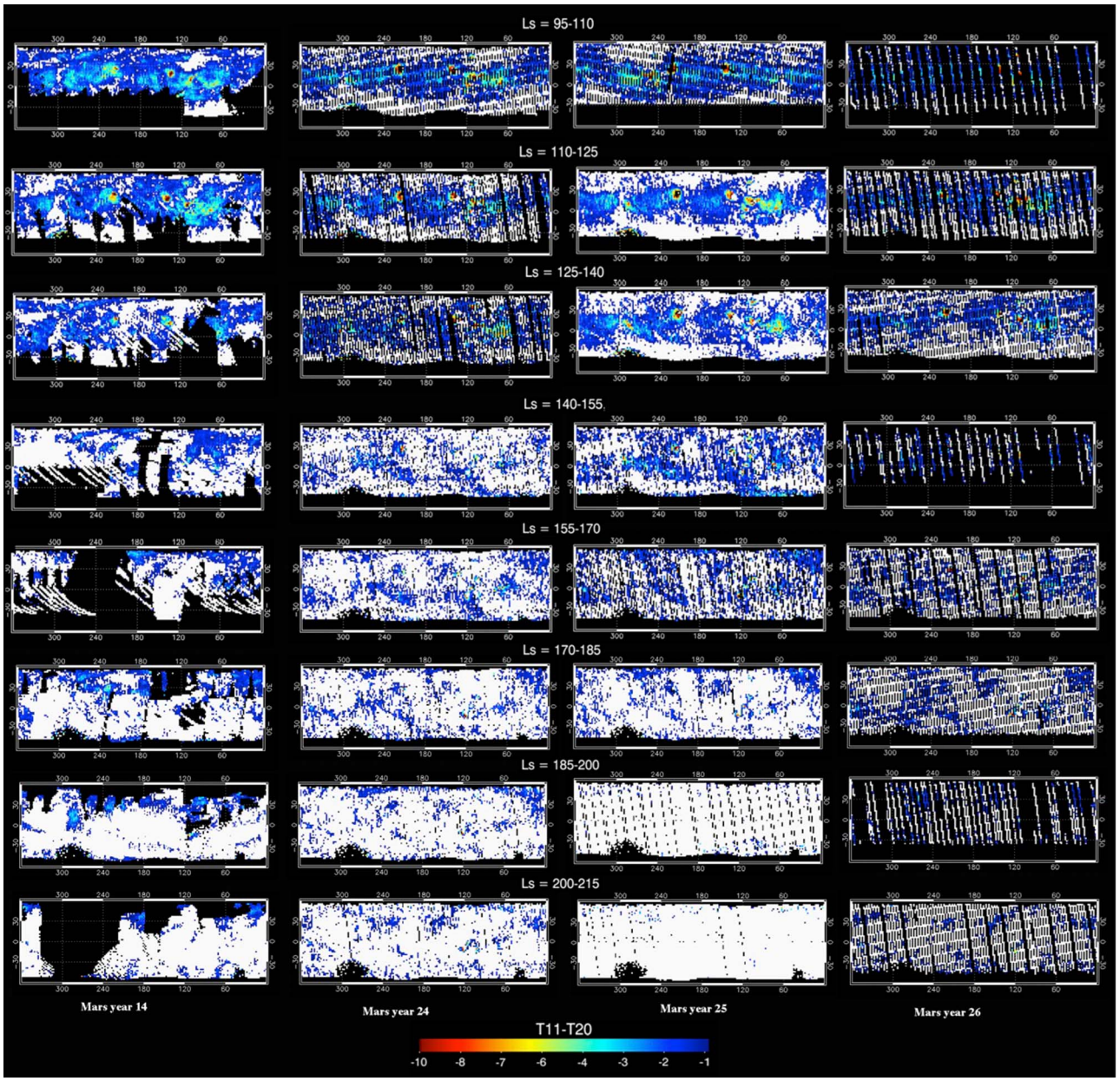

Figure 8a. Water ice cloud maps for Viking year 1 and MGS years 1–3 (Mars year 15, 24–26), L_s = 95–215 (northern summer into northern fall). All maps were generated using a surface model with MGS-derived input parameters. Black areas in maps indicate no data; white areas indicate data, but no cloud signature. Cloud signatures are shown in varying colors, with red (more negative T_{11}–T_{20}) values indicating a stronger signature. We choose to start our map sequence in the L_s = 95–110 bin as the MGS mapping mission began at L_s = 103.

4.1. Northern Summer Period (L_s = 95–170°)

[32] We choose to start our sequence of cloud maps in northern summer (L_s = 95–110°), as that is when MGS TES mapping began (L_s = 103°). We use L_s = 95° as a starting point (as opposed to L_s = 90°, the true solstice) as this is the closest temporal bin to the start of northern summer in our "binning by 15 degrees of L_s" scheme. Water ice clouds are extensive in this period, and tend to be concentrated at low latitudes; obvious clouds over topographic highs are also evident, as well as clouds in Valles Marineris. Mars year 26 has very sparse data in this period, but coverage is more complete in other years. The tropical (aphelion) cloud belt is most pronounced between L_s = 95° and L_s = 140°; thereafter it begins to disperse. This behavior is qualitatively similar to that seen by other researchers [e.g., *Glenar et al.*, 2003; *Liu et al.*, 2003].

[33] Though large-scale cloud behavior appears to be very consistent year-to-year in this time frame (as well as from the Viking era to the MGS one), the smaller-scale behavior changes from year to year. For example, high-latitude clouds seen near longitude 180–240° at L_s = 155–170° in the Viking data and in Mars year 25 are much less pronounced in Mars

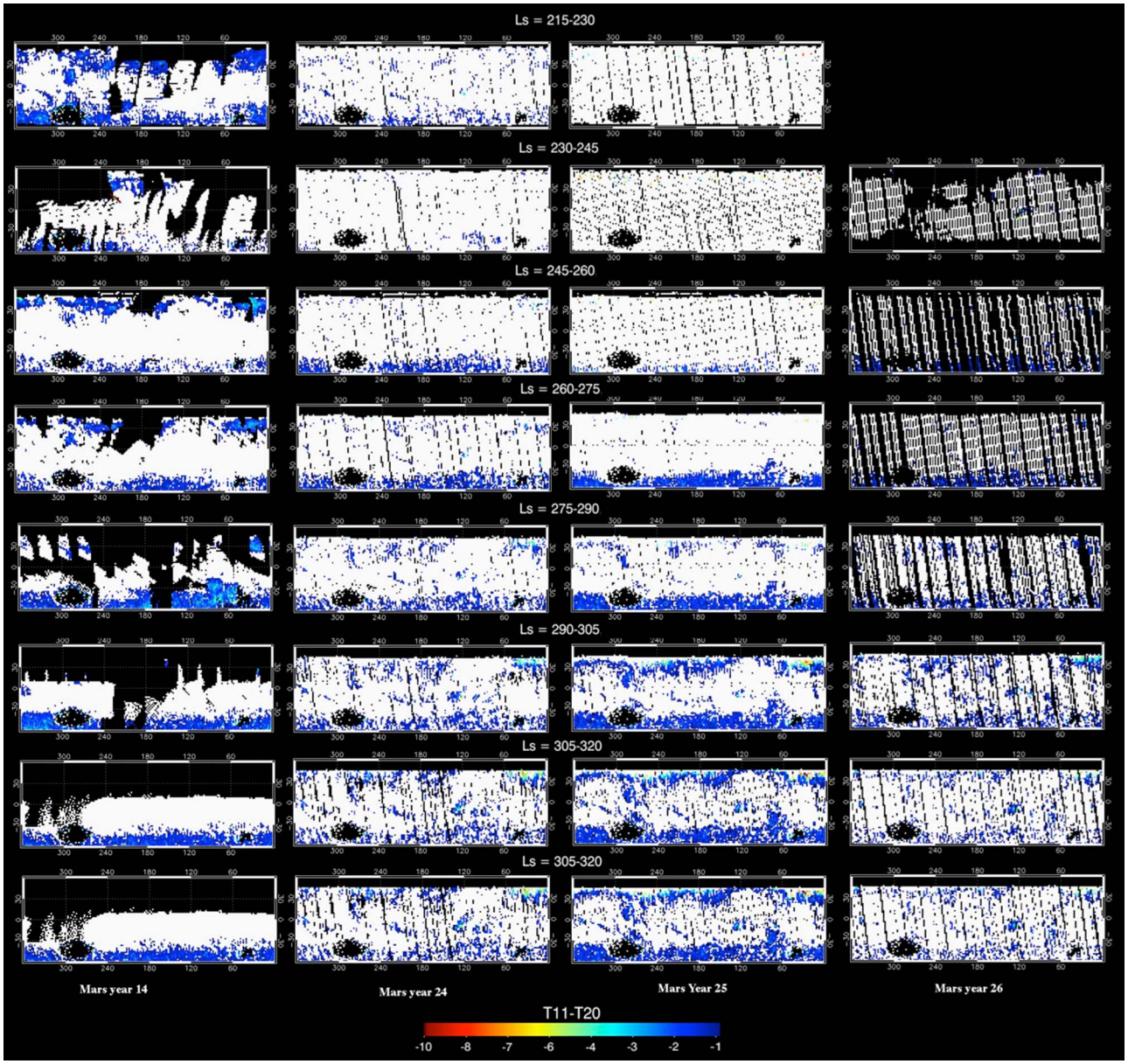

Figure 8b. Water ice cloud maps for Viking year 1 and MGS years 1–3 (Mars year 15, 24–26), L_s = 215–320. All maps were generated using a surface model with MGS-derived input parameters. Black areas in maps indicate no data; white areas indicate data, but no cloud signature. Cloud signatures are shown in varying colors, with red (more negative T_{11}–T_{20}) values indicating a stronger signature.

year 24 and 26. There is also a cloud feature at approximately longitude 60–120° evident at L_s = 140–155° in the Viking data that is largely absent in the MGS years. Overall, the picture is one of consistent climate, with changeable weather.

4.2. Northern Fall Period (L_s = 170–275°)

[34] Northern autumn presents a more complex and varied picture. By L_s = 185°, the aphelion cloud belt has disappeared, and cloud cover at the start of northern fall (L_s = 170–185°) is spotty. The Tharsis volcanoes still show cloud cover, however, and the Viking data shows evidence of high-latitude clouds around longitude = 300° which are not evident in the two MGS years for which we have data. As autumn progresses, high northern latitude clouds become evident in all years; this is the beginning of the polar hood. The extent of the developing polar hood in any particular years does not, of course exactly match that of any other year, but it is always present. There is also a "break" in this developing hood at approximately longitude = 120° in all years, a feature possibly due to winds from Alba Patera. As autumn progresses, the clouds over Tharsis largely dissipate as well, a result consistent with the observations of other researchers (*Wang and Ingersoll*, 2002; *Benson et al.*, 2006).

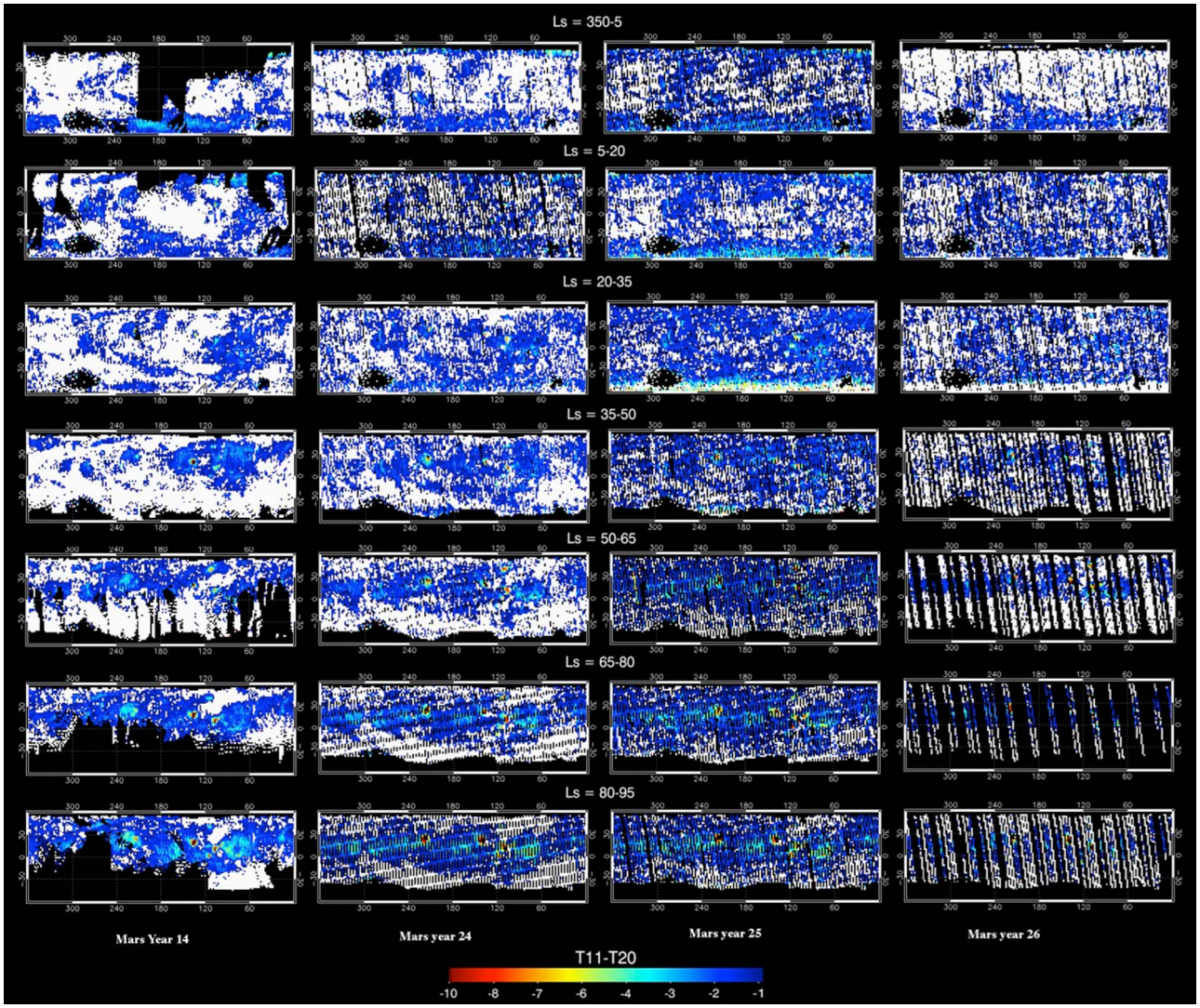

Figure 8c. Water ice cloud maps for Viking year 1 and MGS years 1–3 (Mars year 15, 24–26), L_s = 350–95. All maps were generated using a surface model with MGS-derived input parameters. Black areas in maps indicate no data; white areas indicate data, but no cloud signature. Cloud signatures are shown in varying colors, with red (more negative T_{11}–T_{20}) values indicating a stronger signature.

[35] The Viking data shows a southern hemisphere clouds belt starting at L_s = 215° and continuing through this season. While high dust loading was acknowledged as a potential problem by *Tamppari et al.* [2000], and we have removed high dust locations in this work, this feature remains between L_s = 245°–270°, the time between global dust storms during Viking. It appears to be real water ice cloud detections and have some variability seasonally and year over year.

4.3. Northern Winter Period (L_s = 275–5°)

[36] Northern winter is a fairly quiescent period for water ice cloud activity; this period is characterized by the strong presence of the northern polar hood. Equatorial clouds are almost completely absent, even over topographic highs. High southern latitude clouds are evident in the Viking data, appear much reduced in MY24 and 26, but about the same in MY25. This is the period of the planet-encircling dust storm observed by Viking (L_s = 290°–320°), however, because these clouds are variable in MY24–26, the Viking detections may be valid. In this season, Mars year 25 appears to have somewhat more ice cloud presence than Mars years 24 and 26. The northern polar hood signal weakens around L_s = 350°, and is much less pronounced by L_s = 5°, due to the midlatitude cloudiness increasing and the signal strength of the north polar hood decreasing.

4.4. Northern Spring Period (L_s = 5–95°)

[37] Northern spring is an icy time on Mars. By L_s = 20° the north polar hood has disappeared to above 60° north in most years, as evidenced by no cloud signal at the northernmost extent of the data. But from L_s = 5° to L_s = 50°, low-signal water ice clouds are seen all over the planet, with a greater signal strength in midlatitudes at longitudes =

60–120° in all years. Water ice clouds over the volcanoes become evident again as well, and by L_s = 50° the beginnings of the equatorial cloud belt are seen, again in all years. Mars year 25 still shows more water ice cloud than the other years for which we have data, especially Mars year 26, though data in that year are sparse. In general, northern spring is characterized by the dissipation of the polar hood, and the formation of the tropical cloud belt, and behavior from year to year seems remarkably consistent in timing. Mars year 25 is "icier" than all the others and the Viking year typically has less areal extent of clouds than the MGS years, except perhaps MY26, though the lack of data makes this interpretation difficult. The signal strength is greater for orographic clouds in the MGS years, compared to the Viking year.

4.5. Discussion

[38] The large-scale behavior of Martian water ice clouds does not show much interannual change, either in the short term (MGS year to year), or in the longer term (Viking to MGS). Both eras and all years show the formation and dissipation of the same macrocloud features (tropical cloud belt, polar hoods, clouds over topographic highs) at the same seasons. Small-scale cloud behavior does change from year to year; certain cloud features have different areal extent, appear more or less patchy, and exhibit varying signal strengths. The overall picture is one of a stable climate, with changeable weather, even over 30 Earth year time scales. While it was once thought that the climate on Mars may have changed from the Viking era to the MGS era, that appears not to be the case. However, the interannual differences may provide clues to the effect on the water cycle, given changes in the dust cycle and atmospheric temperatures.

[39] Our results also generally agree with those seen by other researchers studying Martian water ice clouds using different detection and mapping methods.

5. Summary and Conclusions

[40] We have extended use of the method of *Tamppari et al.* [2000] to the MGS TES data set, and have used it to map water ice clouds for three Martian years worth of data. We have also compared our results to the absorption-only optical depths derived by *Smith* [2004], and found that, in general, the results agree well, validating the *Tamppari et al.* [2000] temperature-differencing method for use in assessing water ice cloud climatology. Correlation between the two methods is best with the aphelion cloud belt clouds, and worst with polar hood clouds. As a result of the good correlation between the temperature-differencing method and opacities for the aphelion cloud belt clouds, one can estimate the opacity of the aphelion cloud belt clouds for the Viking era as approximately $\tau_{IR} = -0.048(\Delta w)$.

[41] We have done this study with new, modeled surface output calculated from MGS-derived surface emissivities, albedos, and thermal inertias, and we have compared the TES-based cloud climatology directly with the Viking-based cloud climatology. We have shown that while Martian atmospheric water ice weather changes from year to year, the overall climate with respect to atmospheric water ice is stable. That is, the small-scale cloud behavior is variable year to year, but large-scale behavior is highly repeatable (aphelion cloud belt is seen and appears/disappears near the same seasons in all years, topographic clouds form, and polar hood clouds form near the same seasons in all years). We also have shown that atmospheric water ice is likely more widespread in the Viking era than we previously thought, due to use of our new surface model output, and thus water transport may be occurring on a larger scale than previously thought.

[42] **Acknowledgments.** The authors would like to thank Charles Thompson for invaluable help in developing our IDL code and David Paige for the surface model and access to the source code used to generate it. The authors would like to thank Alexey Pankine for assistance with estimating the range of appropriate cloud temperatures within the TES data set; they would also like to thank Terry Z. Martin and Deborah Bass for many helpful discussions and Ashwin Vasavada for his comments on a draft version of this paper. This work was carried out at JPL/CIT under a grant from the NASA Mars Data Analysis Program. We would also like to thank Sasha Rodin and an anonymous reviewer for their helpful comments and critique, which have greatly improved this manuscript.

References

Arvidson, R. E., K. Deal, B. M. Hynek, F. P. Seelos, M. O. Snider, M. T. Mellon, and J. B. Garvin (2002), Thermal inertia, albedo, and MOLA-derived roughness for terrains in the Terra Meridiani area, Mars, *Lunar Planet. Sci.*, *XXXIII*, Abstract 1748.

Benson, J. L., P. J. James, B. A. Cantor, and R. Remigio (2006), Interannual variability of water ice clouds over major Martian volcanoes observed by MOC, *Icarus*, *184*, 365–371, doi:10.1016/j.icarus.2006.03.014.

Capen, C. F., and L. J. Martin (1971), The developing stages of the Martian yellow storm of 1971, *Bull. 157*, pp. 211–216, Lowell Obs., Flagstaff, Ariz.

Chase, S. C., J. L. Engel, H. W. Eyerly, H. H. Kieffer, F. D. Palluconi, and D. Schofield (1978), Viking Infrared Thermal Mapper, *Appl. Opt.*, *17*, 1243–1251, doi:10.1364/AO.17.001243.

Christensen, P. R. (1998), Variations in Martian surface composition and cloud occurrence determined from thermal infrared spectroscopy: Analysis of Viking and Mariner 9 data, *J. Geophys. Res.*, *103*, 1733–1746, doi:10.1029/97JE02114.

Christensen, P. R., and R. W. Zurek (1984), Martian north polar hazes and surface ice: Results from the Viking survey/completion mission, *J. Geophys. Res.*, *89*, 4587–4596, doi:10.1029/JB089iB06p04587.

Christensen, P. R., et al. (2001), Mars Global Surveyor Thermal Emission Spectrometer experiment: Investigation description and surface science results, *J. Geophys. Res.*, *106*, 23,823–23,871, doi:10.1029/2000JE001370.

Clancy, R. T., et al. (1996), Water vapor saturation at low altitudes around Mars aphelion: A key to Mars climate?, *Icarus*, *122*, 36–62, doi:10.1006/icar.1996.0108.

Clancy, R. T., B. J. Sandor, P. R. Christensen, M. D. Smith, J. C. Pearl, B. J. Conrath, and M. J. Wolff (2000), An intercomparison of ground-based millimeter, MGS TES, and Viking atmospheric temperature measurements: Seasonal and interannual variability of temperatures and dust loading in the global Mars atmosphere, *J. Geophys. Res.*, *105*, 9553–9571, doi:10.1029/1999JE001089.

Clancy, R. T., M. J. Wolff, and P. R. Christensen (2003), Mars aerosol studies with the MGS TES emission phase function observations: Optical depths, particle sizes, and ice cloud types versus latitude and solar longitude, *J. Geophys. Res.*, *108*(E9), 5098, doi:10.1029/2003JE002058.

Curran, R. J., B. J. Conrath, R. A. Hanel, V. G. Kune, and J. C. Pearl (1973), Mars: Mariner 9 spectroscopic evidence for H_2O ice clouds, *Science*, *182*, 381–383, doi:10.1126/science.182.4110.381.

DeMott, P. J., K. Sassen, M. R. Poellot, D. Baumgardner, D. C. Rogers, S. D. Brooks, A. J. Prenni, and S. M. Kreidenweis (2003), African dust aerosols as atmospheric ice nuclei, *Geophys. Res. Lett.*, *30*(14), 1732, doi:10.1029/2003GL017410.

Glenar, D. A., R. E. Samuelson, J. C. Pearl, G. L. Bjoraker, and D. Blaney (2003), Spectral imaging of Martian water ice clouds and their diurnal behavior during the 1999 aphelion season (L_s = 130°), *Icarus*, *161*, 297–318, doi:10.1016/S0019-1035(02)00046-5.

Liu, J., M. I. Richardson, and R. J. Wilson (2002), The response of the Martian circulation or orbital parameter variations, *Eos Trans. AGU*, *83*(47), Fall Meet. Suppl., Abstract P52A-0366.

Liu, J., M. I. Richardson, and R. J. Wilson (2003), An assessment of the global, seasonal, and interannual spacecraft record of Martian climate in the thermal infrared, *J. Geophys. Res.*, *108*(E8), 5089, doi:10.1029/2002JE001921.

Martin, T. Z., A. R. Peterfreund, E. D. Miner, H. H. Kieffer, and G. E. Hunt (1979), Thermal infrared properties of the Martian atmosphere. I - Global behavior at 7, 9, 11, and 20 microns, *J. Geophys. Res.*, *84*, 2830–2842, doi:10.1029/JB084iB06p02830.

Montmessin, F., F. Forget, P. Rannou, M. Cabane, and R. M. Haberle (2004), Origin and role of water ice clouds in the Martian water cycle as inferred from a general circulation model, *J. Geophys. Res.*, *109*, E10004, doi:10.1029/2004JE002284.

Paige, D. A., J. E. Bachman, and K. D. Keegan (1994), Thermal and albedo mapping of the polar regions of Mars using Viking thermal mapper observations: 1. North polar region, *J. Geophys. Res.*, *99*, 25,959–25,991, doi:10.1029/93JE03428.

Palluconi, F. D., and H. H. Kieffer (1981), Thermal inertia mapping of Mars from 60°S to 60°N, *Icarus*, *45*, 415–426, doi:10.1016/0019-1035(81)90044-0.

Pankine, A., L. K. Tamppari, and M. D. Smith (2010), MGS TES observations of the water vapir above the seasonal and perennial ice caps during northern spring and summer, *Icarus*, *210*, 58–71.

Pearl, J. C., M. D. Smith, B. J. Conrath, J. L. Bandfield, and P. R. Christensen (2001), Observations of Martian ice clouds by the Mars Global Surveyor Thermal Emission Spectrometer: The first Martian year, *J. Geophys. Res.*, *106*, 12,325–12,338, doi:10.1029/1999JE001233.

Pleskot, L. K., and E. D. Miner (1981), Time variability of the Martian bolometric albedo, *Icarus*, *45*, 179–201, doi:10.1016/0019-1035(81)90013-0.

Putzig, N. E., M. T. Mellon, R. E. Arvidson, and K. A. Kretke (2003), Thermal inertia analysis of the Martian globe, south polar region, and past landing sites, *Lunar Planet. Sci.*, *XXXIV*, Abstract 1429.

Smith, M. D. (2004), Interannual variability in TES atmospheric observations of Mars during 1999–2003, *Icarus*, *167*, 148–165, doi:10.1016/j.icarus.2003.09.010.

Tamppari, L. K., R. W. Zurek, and D. A. Paige (2000), Viking era water ice clouds, *J. Geophys. Res.*, *105*, 4087–4107, doi:10.1029/1999JE001133.

Tamppari, L. K., R. W. Zurek, and D. A. Paige (2003), Viking-era diurnal water ice clouds, *J. Geophys. Res.*, *108*(E7), 5073, doi:10.1029/2002JE001911.

Wang, H., and A. P. Ingersoll (2002), Martian clouds observed by Mars Global Surveyor Mars Orbiter Camera, *J. Geophys. Res.*, *107*(E10), 5078, doi:10.1029/2001JE001815.

Wilson, R. J., G. A. Neumann, and M. D. Smith (2007), Diurnal variation and radiative influence of Martian water ice clouds, *Geophys. Res. Lett.*, *34*, L02710, doi:10.1029/2006GL027976.

Wolff, M. J., J. F. Bell, P. B. James, R. T. Clancy, and S. W. Lee (1999), Hubble Space Telescope observations of the Martian aphelion cloud belt prior to the Pathfinder mission: Seasonal and interannual variations, *J. Geophys. Res.*, *104*, 9027–9041, doi:10.1029/98JE01967.

D. S. Bass, A. S. Hale, and L. K. Tamppari, Jet Propulsion Laboratory, California Institute of Technology, 4800 Oak Grove Dr., Pasadena, CA 91109, USA. (amy.s.hale@jpl.nasa.gov)

M. D. Smith, NASA Goddard Space Flight Center, Greenbelt, MD 20771, USA.